Li, S., Wang, K., Wang, Y., Jiang, Y., Dosso, S. E. (2018): Geodetically Inferred Locking State of the Cascadia Megathrust Based on a Viscoelastic Earth Model. - *Journal of Geophysical Research*, *123*, 9, pp. 8056—8072.

DOI: http://doi.org/10.1029/2018JB015620

Journal of Geophysical Research: Solid Earth

RESEARCH ARTICLE
10.1029/2018JB015620

Geodetically Inferred Locking State of the Cascadia Megathrust Based on a Viscoelastic Earth Model

Shaoyang Li[1,2], Kelin Wang[3,4], Yanzhao Wang[5], Yan Jiang[3], and Stan E. Dosso[4]

[1]Helmholtz Centre Potsdam, GFZ German Research Centre for Geosciences, Potsdam, Germany, [2]Now at Department of Earth and Environmental Sciences, University of Iowa, Iowa City, IA, USA, [3]Pacific Geoscience Centre, Geological Survey of Canada, Sidney, British Columbia, Canada, [4]School of Earth and Ocean Sciences, University of Victoria, Victoria, British Columbia, Canada, [5]State Key Laboratory of Earthquake Dynamics, Institute of Geology, China Earthquake Administration, Beijing, China

Key Points:
- Widespread interseismic deformation reflects viscoelastic relaxation but may be interpreted as deep locking by elastic models
- Viscoelastic geodetic inversion models indicate megathrust locking at shallow depths at Cascadia
- Regardless of Earth rheology, near-trench ambiguity of locking state can be resolved only by future seafloor observations

Supporting Information:
- Supporting Information S1

Correspondence to:
K. Wang,
kelin.wang@canada.ca

Citation:
Li, S., Wang, K., Wang, Y., Jiang, Y., & Dosso, S. E. (2018). Geodetically inferred locking state of the Cascadia megathrust based on a viscoelastic Earth model. *Journal of Geophysical Research: Solid Earth*, *123*, 8056–8072. https://doi.org/10.1029/2018JB015620

Received 6 FEB 2018
Accepted 26 JUL 2018
Accepted article online 4 AUG 2018
Published online 4 SEP 2018

Abstract In a viscoelastic Earth, stresses slowly built up due to fault locking are relaxed concurrently during the entire interseismic period. This interseismic stress relaxation causes crustal deformation much farther away from the locked fault than can be explained using elastic models that neglect the relaxation. Here we develop a viscoelastic geodetic inversion model to address this problem at Cascadia. We invert ~500 horizontal velocity vectors based on continuous and campaign geodetic measurements over the past two decades. Ambiguities arising from long-term rotation of upper-plate crustal blocks are addressed by test-correcting the geodetic velocities with two different block-motion models. Fault back slip (i.e., slip deficit) Green's functions are derived using a Maxwell viscoelastic finite element model with realistic subduction zone structure and megathrust geometry. The preferred model features a narrow and shallow megathrust locked zone, consistent with earlier thermorheological reasoning. For an elastic model to fit the data to the same fidelity, megathrust locking has to extend to much greater depths. However, even with the viscoelastic model, the land-based geodetic data still cannot resolve whether there is some creep (incomplete locking) in the shallowest part of the megathrust far offshore. Neither can the land data fully resolve along-strike variations of the locking state. These ambiguities can be resolved only when adequate seafloor geodetic data are obtained.

1. Introduction

The Cascadia subduction zone, where the Juan de Fuca plate subducts beneath the North America (NA) plate, has produced great megathrust earthquakes in the past (Atwater, 1987; Goldfinger et al., 2017). The last event occurred in A.D. 1700 (Satake et al., 2003), and the margin is presently in a late stage of interseismic strain accumulation toward the next event. Contemporary geodetic observations provide unambiguous evidence that the megathrust is currently locked to some degree (e.g., Henton, 2000; Khazaradze et al., 1999; Mazzotti et al., 2003; McCaffrey et al., 2013; Miller et al., 2001; Savage et al., 1991; Schmalzle et al., 2014), but it is unclear whether it is fully locked and how far downdip the locked zone extends. The working hypothesis of full locking of a narrow segment at shallow depths, as is featured in many of the Cascadia locking models, is consistent with the warm thermal state of the subduction zone and the paucity of interplate seismicity at present (see review by Wang & Tréhu, 2016). To constrain geodetically the locking state of the Cascadia megathrust, understanding the effect of interseismic viscoelastic stress relaxation and making near-field, seafloor observations are among the most important requirements.

The main objective of this work is to address the issue of interseismic stress relaxation by inverting geodetic observations using a three-dimensional viscoelastic finite element model. Although the study, like any other studies at present, cannot uniquely define the locking state of the Cascadia megathrust, it helps to minimize a major source of uncertainty. More importantly, the results have significant global implications. The vast majority of megathrust locking models worldwide assume an elastic Earth model and may be affected by similar uncertainties in resolving the downdip distribution of locking. The results presented here represent a case study to illustrate the problem and to suggest a strategy to solve it. A secondary objective is to document ambiguities of the locking models, even with the improved Earth rheology, to provide guidance for future research such as making seafloor geodetic observations.

All the basic concepts regarding viscoelastic earthquake-cycle deformation in subduction zones have been well established over the past five decades (e.g., Bott & Dean, 1973; Cohen, 1984; Elsasser, 1969; Matsu'ura

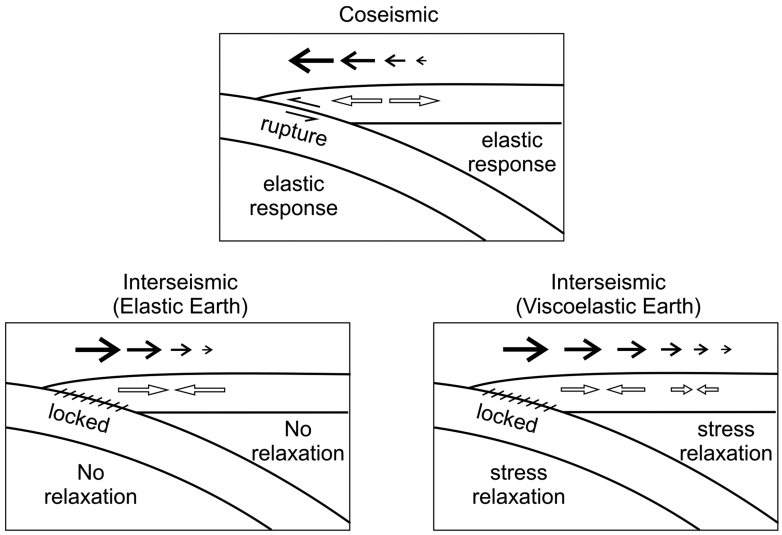

Figure 1. Cartoon illustration of the role of mantle rheology in controlling surface deformation due to fault slip or locking. (top) In coseismic deformation, the mantle response is elastic. (bottom left) In a hypothetical elastic Earth, interseismic deformation is a mirror image of coseismic deformation. (bottom right) In a viscoelastic Earth, stress relaxation causes wide spread upper-plate deformation if the megathrust has been locked for a long time. The black arrows represent surface displacement or velocity. The opposing hollow arrows represent strain or strain rates.

& Sato, 1989; Miyashita, 1987; Savage, 1983; Thatcher & Rundle, 1984; Wang, Hu, et al., 2012). For the focus of the present paper, it is important to emphasize that viscoelastic stress relaxation is not limited to postseismic deformation shortly after the earthquake. Long after the earthquake, even if the stress induced by the earthquake is nearly fully relaxed, stresses built up due to the locking of the megathrust are being relaxed at the same time, regardless of whether the deformation rate is still changing with time (Wang, Hu, et al., 2012).

Figure 1 illustrates the main difference between elastic and viscoelastic models. In a hypothetical elastic Earth, if the interseismic locked zone is assumed to be the same as the coseismic rupture zone, the resultant surface deformation is simply a subdued mirror image of coseismic formation, confined to be close to the locked fault. In a viscoelastic Earth, provided that the fault has been locked for a long time and that the locked zone is long in the strike direction, the same megathrust locking can cause surface deformation much farther away from the locked fault because of stress relaxation in the mantle. This widespread deformation is commonly observed at subduction zones that are in a late stage of interseismic locking, such as the Japan Trench prior to the 2011 moment magnitude (M_w) 9 Tohoku-oki earthquake and Cascadia at present. If the observed deformation is to be explained using an elastic model, megathrust locking has to be incorrectly assumed to extend to large depths, a common problem in pre-Tohoku-oki locking models (Wang et al., 2018). For Cascadia, Wang et al. (2003) purposely introduced deep locking, referred to as "effective transition," in order to account for the missing effect of viscoelastic relaxation in an elastic model.

Three-dimensional viscoelastic deformation models have been used to model contemporary crustal deformation at Cascadia, but the models presented in this paper are the first finite element-based geodetic inversion models for this subduction zone. Earlier finite element viscoelastic models such as those in Wang et al. (2001) and Wang, Hu, et al. (2012) are forward models designed to explain the first-order pattern of geodetic observations. The inverse viscoelastic models of Pollitz and Evans (2017) are based on analytical solutions that necessarily simplify the Earth structure such as not including a subducting slab. Compared to the work of Pollitz and Evans (2017), our study is more process-focused and designed to address the main theme illustrated by Figure 1.

2. Geodetic Data

In this study, we invert decade-scale velocities of continuous and campaign Global Navigation Satellite System (GNSS) sites reported by McCaffrey et al. (2013). The effect of episodic slow slip around the mantle-

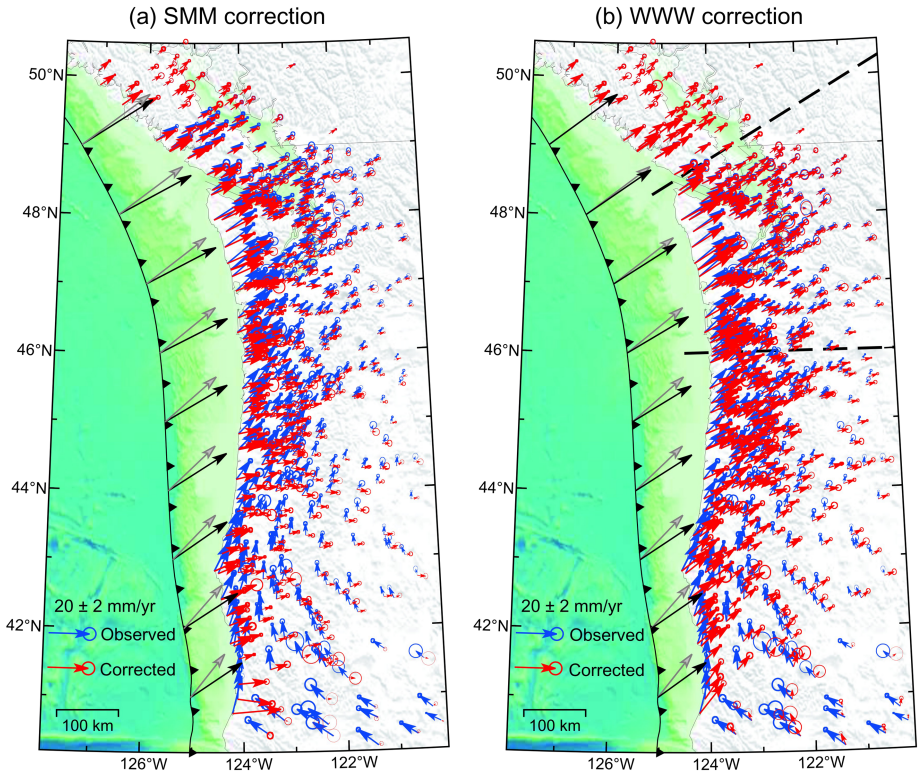

Figure 2. Raw Global Navigation Satellite Systems data (blue) and data corrected with two crustal block models (red). (a) Correction using the SMM block model (block boundaries not shown) (Schmalzle et al., 2014). (b) Correction using the WWW block model (the black dashed lines are block boundaries; Wang, Wang, et al., 2012). In both models, the gray arrows along the deformation front are Juan de Fuca-North America convergence vectors from DeMets et al. (2010), and the black arrows are subduction rate vectors after the block-motion correction.

wedge corner (roughly 30–40 km depth; Dragert et al., 2001; Gao & Wang, 2017; Rogers & Dragert, 2003) is averaged out in deriving the decadal velocities and thus does not affect the inversion results. For determining the locking state of the Cascadia megathrust, we invert the horizontal components of the >500 GNSS sites west of 120°W (Figure 2). The vertical component generally has a smaller signal-to-noise ratio, and the geological processes contributing to the vertical deformation other than megathrust locking are often poorly understood (Wang & Tréhu, 2016).

All the GNSS velocities are defined with respect to a stable NA reference frame and thus can be directly compared to finite element modeling results obtained with fixed far-field boundaries. The observed velocity field (blue vectors in Figure 2) shows that parts of the upper plate rotate clockwise with respect to the stable NA plate. In the fore arc, especially south of 46°N, the rotation results in considerable margin-parallel northward motion. This long-term geological deformation, assumed to be independent of megathrust earthquake cycles, has been modeled as "block motion" (McCaffrey et al., 2007, 2013; Wells et al., 1998; Wells & Simpson, 2001). Both the secular block motion and interseismic megathrust locking contribute to contemporary crustal deformation, but it is very challenging to distinguish the two contributions from the available GNSS data (Wang & Tréhu, 2016).

Despite the challenge, McCaffrey et al. (2007), McCaffrey et al. (2013), and Schmalzle et al. (2014) simultaneously estimated block motion parameters and megathrust locking by inverting geodetic observations using an elastic Earth model. We take a simpler approach in this work. We first subtract the bock motion signal from the GNSS data and then invert the "corrected" GNSS data to infer megathrust locking. This is a valid approach because the block-motion correction in most places removes a rigid-body velocity field, but the estimation of megathrust locking state depends heavily on spatial velocity gradients (strain rates). For estimating the effect of interseismic viscoelastic relaxation, the velocity gradients are the most essential. Even

if the block-motion model used for the correction contains uncertainties, much of the important information is still in the corrected GNSS data.

To explore how the uncertainties in the block-motion correction affect our results, we correct the GNSS velocities with two very different block-motion models and compare their subsequent inversion results. One of these is the model of Schmalzle et al. (2014) based on the work of McCaffrey et al. (2007) and McCaffrey et al. (2013), referred to as the SMM block model. The other is the model of Wang, Wang, et al. (2012) based on the work of Wells et al. (1998) and Wang et al. (2003), referred to as the WWW model. The SMM model divides the upper plate into 28 blocks each having its own Euler vectors. The WWW model divides the upper plate into three blocks separated by two straight boundaries (Figure 2b). The block in the south rotates clockwise with respect to NA (Euler pole at 49.454°N, 242.7853°E, rotation rate −0.4139°/Ma), and the block in the north has no rotation (Wang, Wang, et al., 2012). Across the zone in the middle, the deformation rate changes linearly between these two blocks.

Because of block rotation, local subduction rate can be different from the Juan de Fuca-NA convergence rate. It is the local subduction rate that is relevant to megathrust locking and creep. For the simpler WWW model, the subduction rate is readily calculated from the Euler vectors. For the SMM model, we derive subduction rates from the velocities of GNSS sites predicted by the rigid-block rotation models made available to us by G. Schmalzle (personal communication, 2017). In both cases, the subduction rates vary along strike, typically close to 40 mm/yr in southern British Columbia and Washington and smaller further south, as shown in Figure 2. Our model also includes northernmost Cascadia (off central Vancouver Island), where the Explorer plate is subducting at a rate of 20 mm/yr beneath NA, although there are very few GNSS sites to constrain the locking state here. Errors in the subduction rates introduced by block-motion correction are difficult to quantify. Because the correction becomes larger generally from north to south (Figure 2), we expect that the errors in their resultant subduction rates also increase southward. The inversion results presented in the following sections are based mainly on the SMM model, but the results based on the WWW model will also be discussed.

3. Inversion Procedure

3.1. Finite Element Model

The finite element model used in this study is constructed using software PyLith (Aagaard et al., 2013). Our model consists of four domains (Figure 3a): the continental plate, the oceanic plate, the continental mantle including the mantle wedge, and the oceanic mantle. For comparison purposes, we have constructed both elastic and viscoelastic versions of the models. In the viscoelastic version, the two convergent plates are assumed to be elastic, but the mantle is assumed to be viscoelastic. Because we are dealing with interseismic deformation a few hundred years after a great earthquake, the transient rheology as represented by a biviscous Burgers material (Pollitz, 2003; Wang, Hu, et al., 2012) is considered unimportant, and we assume a Maxwell mantle rheology. Following the study of Wang, Hu, et al. (2012), the thicknesses of the oceanic and continental plates are set to be 30 and 40 km, respectively, and the Maxwell viscosities of the continental and oceanic mantle are assumed to be 10^{19} and 10^{20} Pa s, respectively. The rigidity values of the elastic plates and the mantle are assumed to be 48 and 64 GPa, and the Poisson ratio is assumed to be 0.25 throughout the model domain. The Maxwell relaxation times (viscosity divided by rigidity) of the continental and oceanic mantle are thus about 12 and 120 years, respectively.

The western and eastern model boundaries, both about 1,200 km from the subduction zone, and the bottom boundary at 500 km depth are anchored boundaries (zero displacements). The northern and southern boundaries, both about 700 km from the subduction zone, are free boundaries (zero stress). The top boundary is also free. We use controlled meshing to let element size vary gradually with space. Small elements (about 15 km) are used for the continental and oceanic plates, and even smaller elements (about 10 km) are used near the trench. Large elements (up to 50 km) are used for the deep part of the mantle (Figure 3a). For the megathrust geometry, we adopt the model compiled by Gao (2016) for which the depth contours are shown in Figure 4. This model is a combination of a few geometrical models including those of McCrory et al. (2012) for southern Cascadia, McCrory et al. (2004) for northern Cascadia, and Gao et al. (2017) for northernmost Cascadia based on megathrust low-frequency-earthquake location information from Royer and Bostock (2014).

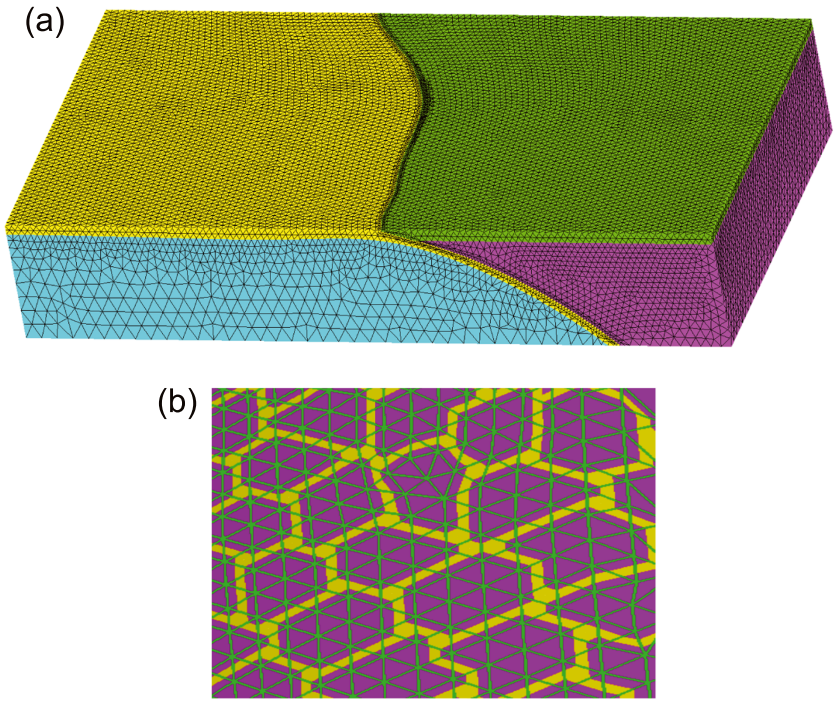

Figure 3. Configurations of the finite element model. (a) Finite element mesh and four model units: Oceanic plate (yellow), continental plate (green), oceanic mantle (light blue), and continental mantle (purple). See Figure 4 and other figures for depth contours of the plate interface. (b) A part of the fault to illustrate patches (outline by thick yellow lines) for which average back slip rate vectors are determined by the inversion. The green lines are mesh lines along the fault (each element is about 10 km across).

Interseismic fault locking is simulated using the back slip method (Savage, 1983), that is, the fault slip slowly in the opposite sense to subduction. The locking ratio is defined as the ratio of the back slip rate to the subduction rate. Full locking is accomplished by having a back slip rate equal to the subduction rate (locking ratio = 1). The state of no locking (full-speed creep) is accomplished by having zero back slip rate (locking ratio = 0). The back slip model addresses the deformation field due only to fault locking, with the long-term, background field assumed to have been subtracted (Savage, 1983). One can also design models that include both the background field and earthquake-cycle deformation (e.g., Wang et al., 1994), but there are long-standing unresolved difficulties in dealing with the asymmetry of coseismic and interseismic deformation in a viscoelastic Earth (Wang, 1995). A better understanding of the entire physical process combined with advanced numerical modeling (e.g., Sobolev & Muldashev, 2017; van Dinther et al., 2013) may eventually overcome such difficulties. For the inversion exercise in this work, we prefer the simpler back slip approach.

3.2. Inversion Method

The finite element model described above establishes the following linear system relating surface deformation to fault locking (back slip) at a late stage of the interseismic phase when deformation rate no longer changes with time,

$$G \cdot \mathbf{s} = \mathbf{d}$$

where **s** is the parameter vector containing back slip rates and **d** is the data vector containing GNSS velocities shown in Figure 2. The matrix G depends on the model geometry, material properties, and the numerical structure of the finite element model. Our task is to invert this system to determine **s** from **d**. We perform the linear inversion using MATLAB routine lsqlin, a subspace trust region method based on the interior-reflective Newton method (Coleman & Li, 1996). In this inversion method, the data are weighted by their errors expressed as variances.

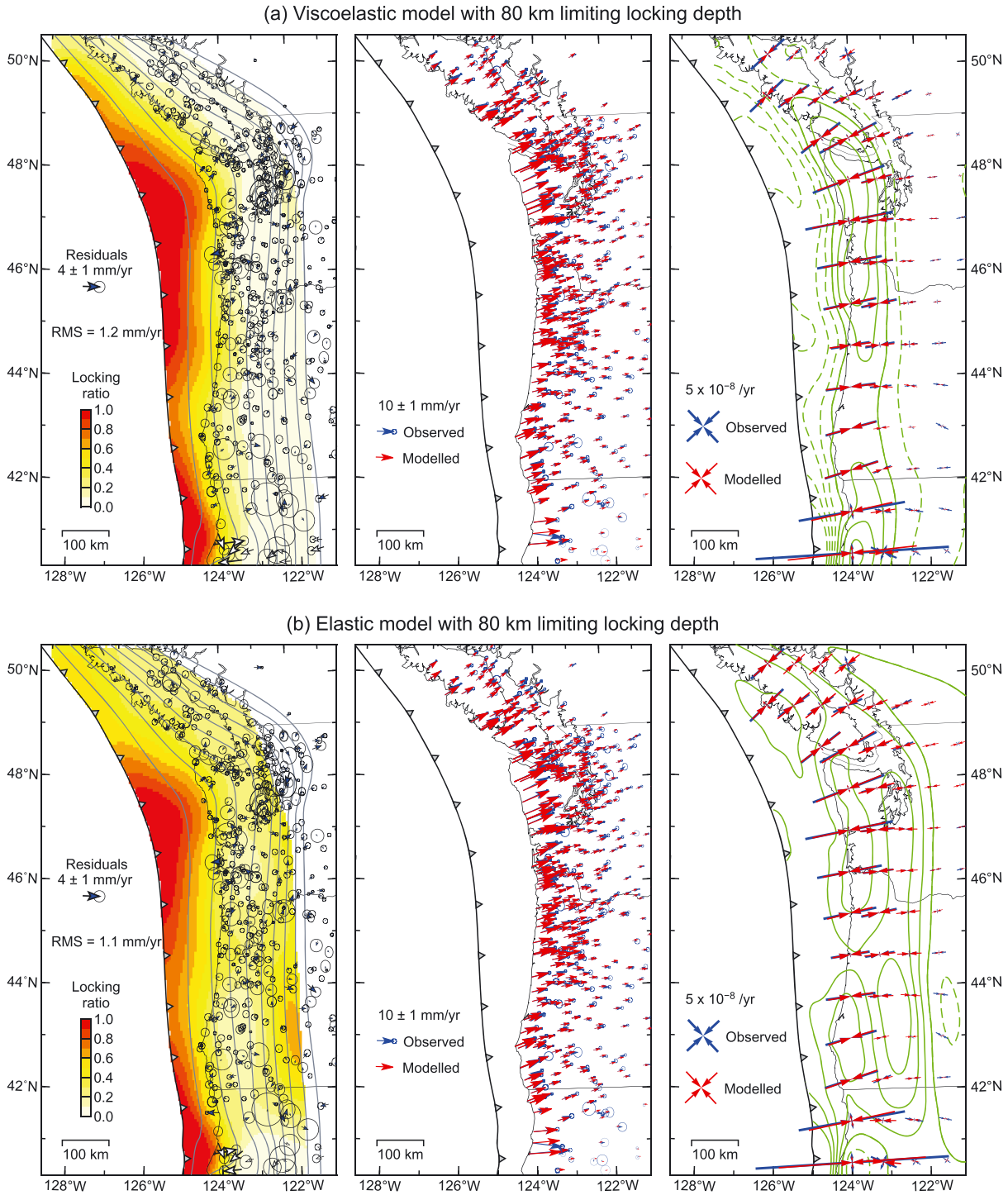

Figure 4. Map view of preferred viscoelastic locking model in comparison with a corresponding elastic model with the same inversion parameters (Table 1). (a) Results of the viscoelastic model. (b) Results of the elastic model. In both a and b, the three panels from left to right are locking ratio and Global Navigation Satellite Systems (GNSS) residuals, observed and model GNSS velocities, and observed and model strain rates plus predicted uplift rates contoured at 1 mm/yr interval (green curves with subsidence dashed). GNSS residuals of sites in the southernmost area (hollow arrows) are not used in the calculation of the root-mean-square (RMS) residual. In the left panels and all similar maps in this paper, megathrust depth is contoured using gray lines at 10-km interval.

In the finite element model, each nodal point on the megathrust fault has a back slip (rate) vector. For convenience in the inversion, we reduce the number of back slip vectors by collecting nearby fault nodes into groups to form patches of uniform locking as illustrated in Figure 3b. Elements along the fault surface are

triangular and about 10 km in size and even smaller near the deformation front. Across each of the elements shared by neighboring slip patches (those crossed by the thick yellow line in Figure 3b), the back slip rate (and direction) changes from the uniform value of one patch to the uniform value of the next patch. In total, we have 235 fault patches from the deformation front to 80 km depth, much deeper than any physically reasonable seismogenic depth. The patches are roughly 30–40 km in size but much smaller, ~10 km, near the deformation front. We then generate our "Green's functions," that is, late-interseismic velocities at all the GNSS sites caused by unit back slip of the two components (dip and strike) of these patches. In the forward simulation to generate the Green's functions, the unit back slip vectors at different nodes in the same patch may have slightly different rake values because of slight variations in fault geometry within the patch. The inversion only determines a single back slip vector for the average strike and dip directions of each patch.

For the elastic Earth model, the problem is similar to any other geodetic inversion model using the Okada (1992) solution. The finite element solution differs from the Okada (1992) solution mainly in allowing spatial variations in material properties as mentioned above, but this is of very minor significance given the uncertainties in the data and other parameters. For the viscoelastic Earth model, we run the Green's function simulations to 300 years when the deformation no longer exhibits significant change with time. This is 25 times the 12-year continental-mantle Maxwell time but only 2.5 times the oceanic-mantle Maxwell time. We would prefer a longer time span or even to the steady state, but given the difficulty of using larger time steps a very long time after the initial loading in the currently used code, adding another 200 years or more simulation would make the Green's function computation extremely time consuming. However, our test runs with various locking scenarios show that the results at 500 years are similar to those at 300 years for the viscosity values we use (see Figure S1 in the supporting information). This indicates that the time dependency of upper plate deformation is controlled mainly by the lower viscosity (smaller Maxwell time) of the continental mantle. Note that the Green's function obtained this way does not include contributions from earlier earthquake cycles. It is difficult to know how important these earlier contributions are in real Earth, and it is difficult to know whether published theoretical predictions using kinematically assigned earthquakes and/or two-dimensional models reflect the actual process. Nevertheless, this simplified procedure potentially gives rise to some uncertainties that are difficult to quantify.

To cope with the intrinsic nonuniqueness and instability of the inverse problem, we need to impose various constraints to the 235 back slip rate vectors to be determined by the inversion. One type of constraint is the limiting locking depth (LLD), below which the megathrust is assumed to be creeping at the full subduction rate (zero back slip). As we will show subsequently, this constraint is important if a purely elastic Earth model is used but is hardly needed if a viscoelastic model is used.

Another type of constraint is the boundedness of the back slip rates, which in our inversion is given in the form of upper and lower bounds. The bounds are imposed differently for the local dip and strike components of the back slip vectors. In the dip direction, we typically allow the back slip rate to vary between 0 (full creep) and 40 mm/yr (full locking) for the fault area shallower than the LLD and let the inversion determine the optimal value for any patch within this area. Because subduction rates generally decrease southward (Figure 2), a uniform upper bound of 40 mm/yr implies a southward increase in the tolerance of errors in the subduction rates. This is fortuitously consistent with the expectation of southerly increasing errors in subduction rates discussed in the Introduction. The back slip rates determined by the inversion may thus be slightly larger than the subduction rate in very limited area. In some testing cases, we set the upper bound to a smaller value such as 0 or 20 mm/yr only for the shallowest, near-trench patches to enforce interseismic trench creep. The bounds for the strike component not only affect the magnitude of the back slip rate but also control its direction. Given the slight northward obliquity of subduction, we set the bounds for the strike component to very small positive values (0–10 mm/yr), so that the back slip is only slightly oblique to the local dip direction. We use a small range instead of a constant value because the local subduction direction exhibits some along strike variations, even after the correction for the upper-plate block motion is made (Figure 2).

A third type of constraint is the smoothness of the back slip distribution along the fault surface. The smoothness is introduced using the Laplacian smoothing constraints, which minimize differences between back slip rate vectors of neighboring fault patches (Wald & Heaton, 1994). In the inversion, the smoothness is

Table 1
Model Parameters

Figure number	Mantle rheology (elastic or viscoelastic)	Block motion model	Limiting locking depth (km)	Smoothness factor	Maximum back slip at trench (mm/yr)
4a	V	SMM	80	400	40
4b	E	SMM	80	400	40
5a	V	SMM	30	400	40
5b	E	SMM	30	400	40
6a	V	SMM	80	400	20
8a	V	SMM	80	1600	40
8b	V	SMM	80	100	40
8c	V	SMM	30	40	40
10a	V	WWW	80	400	40
10b	V	WWW	30	400	40
10c	V	WWW	80	400	20

controlled by a smoothness factor β. A larger β value results in a smoother distribution. As is well known, there is a trade-off between the model smoothness and the preciseness of data fit. A very precise fit to the GPS data may require a very small β, thus producing a rugged locking pattern which may be unphysical. The optimal smoothness factor is often subjectively chosen and reflects the researchers' own understanding of the physics of megathrust locking.

The vector difference $\mathbf{v}_{res\_j} = \mathbf{v}_{obs\_j} - \mathbf{v}_{mod\_j}$ between the observed velocity $\mathbf{v}_{obs\_j}$ and the model-predicted velocity $\mathbf{v}_{mod\_j}$ at the jth GNSS site is called the GNSS residual for that site. As a measure of the overall "goodness" of data fit, we define a root-mean-square (RMS) residual as follows.

$$\mathrm{RMS} = \sqrt{\frac{1}{n}\sum_{j=1}^{n}\left|\mathbf{v}_{res\_j}\right|^2}$$

where n is the number of sites. Several GNSS sites south of 41°N suffer from large uncertainties; velocity values vary drastically between nearby sites (Figure 2). We have included these sites in the inversion but excluded them from the calculation of the RMS residual. The RMS residual is by no means a sufficient measure of the validity of the results. Because of the notorious nonuniqueness of inversion problems, many models can yield similarly small RMS residual values. In the following section, we will demonstrate that the effect of viscoelastic relaxation can be unambiguously resolved despite the nonuniqueness.

4. Results and Discussion

4.1. Importance of Interseismic Stress Relaxation

Because of viscoelastic relaxation, interseismic crustal deformation occurs far away from the locked zone (Figure 1). To understand fault locking with a realistic Earth rheology, it is important to derive a solution that explains the long wavelength deformation pattern. When comparing the performance of elastic and viscoelastic models, we invert the same (block-motion-corrected) GNSS data using the same inversion constraints, so that the only difference between models is Earth rheology. Using the locking patterns (back slip vectors) determined by the inversion, we then calculate the predicted surface displacements, strain rates, and RMS residuals. We should reiterate that a nonzero locking ratio does not always indicate mechanical locking and stress buildup but only portrays a kinematic state of no slip or slower slip than subduction rate, referred to as "apparent locking." A patch of the fault may not be creeping at full rate simply because it is in the stress shadow of a mechanically locked neighboring patch, and for this reason the "downdip limit" of true mechanical locking cannot be clearly defined by these models (Wang & Tréhu, 2016).

Figure 4 shows our preferred viscoelastic model and the corresponding elastic model, which were both obtained by inverting the SMM block-motion-corrected GNSS data with the same inversion constraints. The inversion constraints are (Table 1) LLD = 80 km, smoothing factor β = 400, and maximum back slip rate at trench of 40 mm/yr. In the results of the viscoelastic locking model (Figure 4a), the area of high locking ratio (>0.6) is shallower than 20 km, in qualitative agreement with the viscoelastic models of Pollitz and Evans (2017). How the locking ratio decreases further downdip cannot accurately reflect how the frictional behavior or true mechanical locking varies in the dip direction because of the above-mentioned stress-shadowing effect. There are some along-strike variations in the degree of locking, with limited creeping off northern Vancouver Island and southern Oregon, but the pattern of locking-creeping variations is not unique as will be further discussed in section 4.3.

The shallow locking featured by both models in Figure 4 is consistent with the young age of the subducting plate and hence the warm thermal regime of this subduction zone (Hyndman & Wang, 1993; Wang & Tréhu, 2016). It is also consistent with the notion that the megathrust seismogenic zone is located mostly offshore, as can be inferred from the predominance of coastal subsidence in ancient great earthquakes (Atwater & Hemphill-Haley, 1997; Leonard et al., 2010; Wang et al., 2013). The results also confirm the spatial

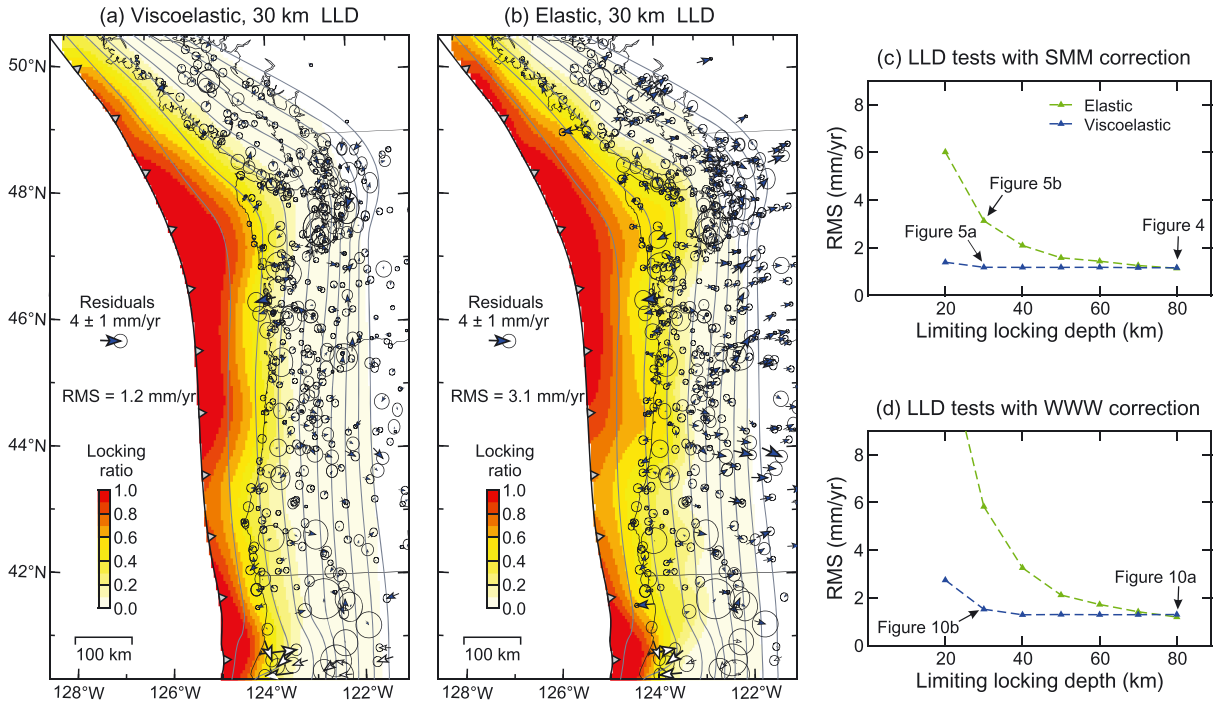

Figure 5. Model results showing the effects of limiting locking depth (LLD) allowed in the inversion. (a and b) Locking ratios and Global Navigation Satellite Systems (GNSS) residual of a viscoelastic model and its corresponding elastic model, respectively, both with a 30-km LLD (Table 1). See Figure 4 for explanation of hollow arrows in the southernmost part of the map area. (c and d) Root-mean-square (RMS) residual of GNSS data fit as a function of LLD for models obtained by inverting the SMM-corrected data (Figure 2a) and WWW-corrected data (Figure 2b) data, respectively. Except for the LLD value, all the other inversion parameters are the same as for the model of Figure 4a.

separation of the seismogenic zone and the zone of episodic tremor and slip, an important issue of fault zone rheology and dynamics discussed by Gao and Wang (2017). See Figure S2 for a comparison with the tremor distribution reported by Wells et al. (2017). However, in the elastic version (Figure 4b), there is also significant locking (locking ratio ~0.4) all the way down to the LLD of 80 km allowed by the model. If the LLD were greater than 80 km, this "partial locking" would extend to even greater depths. The reason is, as explained in section 1 (Figure 1), that the elastic model had to incorrectly invoke deep locking in order to fit far-field surface deformation that is actually caused by interseismic viscoelastic stress relaxation.

Both models shown in Figure 4 feature similarly good fit to GNSS velocities (RMS residual 1.1–1.2 mm/yr), but the model-predicted vertical deformation patterns show some differences (right panel of Figures 4a and 4b). One might think that the vertical component of the GNSS data could provide additional and diagnostic information to constrain the inversion. However, as discussed by Wang and Tréhu (2016), there are a number of known or unknown tectonic or nontectonic processes that contribute to crustal tilt at a variety of time scales. As a result, scientists understand the physics of how the crust is strained (horizontal deformation) much better than how it is tilted (vertical deformation) in the interseismic phase of the earthquake cycle. It is not clear how much of the observed tilt is actually associated with interseismic locking of the megathrust. The problem is compounded by the fact that errors in the vertical component of GNSS data are typically a factor of three larger than in the horizontal component, yet the vertical deformation signal due to megathrust locking at Cascadia is usually smaller than the horizontal signal by much more than a factor of three (Wang & Tréhu, 2016). We do not think current vertical observations can better constrain fault locking.

Because the deep locking seen in Figure 4b is obviously unphysical, we devise models with a shallower LLD to see if the situation can be improved. The models shown in Figures 5a and 5b are derived by imposing an LLD of 30 km, but other model parameters are the same as for the models of Figures 4a and 4b, respectively (Table 1). With the shallower LLD, both the viscoelastic and elastic models yield locking patterns similar to the preferred model (Figure 4a). The comparison between Figures 4a and 5a indicates that the LLD is an unimportant constraint for the viscoelastic model. For the elastic model, although the shallower LLD results in a physically more reasonable locking pattern, it also results in a much worse fit to the GNSS data, with an

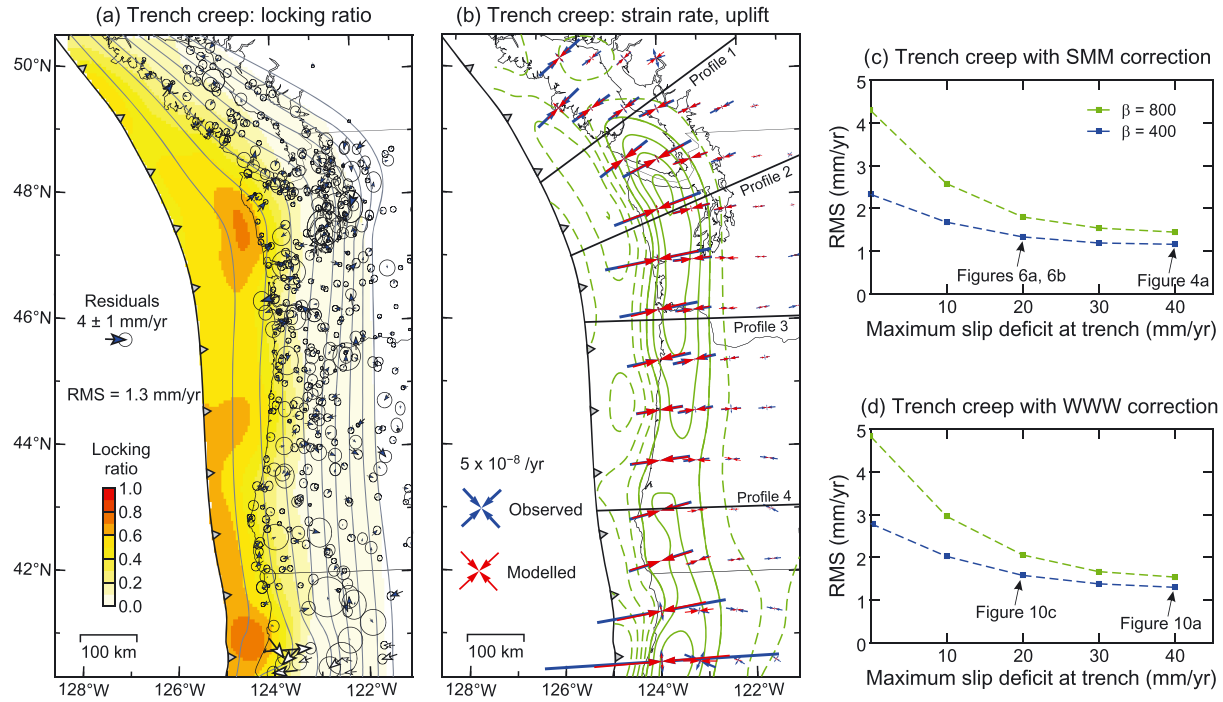

Figure 6. Viscoelastic model results showing the effects of enforcing some fault creep at the deformation front. (a) Locking ratio and Global Navigation Satellite Systems (GNSS) residuals for a viscoelastic model with back slip rates at deformation front limited to 20 mm/yr. All the other inversion parameters are identical to those for the model of Figure 4a (Table 1). (b) Strain rates plus predicted uplift rates contoured at 1 mm/yr interval (green curves with subsidence dashed) for the same model as in (a). The straight black lines mark the locations of the margin-normal profiles used for Figure 7. (c and d) Root-mean-square (RMS) residual of GNSS data fit as a function of allowed maximum back slip (i.e., slip-deficit) rate for viscoelastic models obtained by inverting the SMM-corrected data (Figure 2a) or WWW-corrected data (Figure 2b), respectively. Except for the enforced trench creep and the β values shown, all the other inversion parameters are the same as for the model of Figure 4a.

RMS residual of ~3.1 mm/yr (Figure 5b). The large misfit occurs nearly exclusively in the far-field (Figure 5b). It arises because the shallow locking in an elastic Earth model can produce surface deformation only near the locked zone and is unable to explain the observed long-wavelength, far-field deformation that is actually caused by interseismic stress relaxation (Figure 1). Given the same imposed locking distribution, forward elastic models systematically predict lower surface velocities in the far field than do viscoelastic models (Figure S3). Similar far-field misfit is often seen in elastic locking models elsewhere, and the residual is often incorrectly attributed to long-term geological motion such as back-arc shortening (Li et al., 2015; Wang, Hu, et al., 2012).

Figures 5c and 5d further illustrate how the model fit to GNSS data is affected by the imposed LLD for a series of viscoelastic and elastic models based on inverting either the SMM-corrected or WWW-corrected GNSS data. The other inversion parameters for these models are the same as for the models shown in Figure 4. The results show that, regardless of which block-motion model is used to correct the GNSS data, the viscoelastic model results are insensitive to the LLD if the value is 30 km or larger, but the elastic models are very sensitive to this constraint.

4.2. Near-Trench Ambiguity

Because of lack of seafloor geodetic observations, the locking state of the Cascadia megathrust far offshore cannot be uniquely determined. As shown by Schmalzle et al. (2014) using an elastic Earth model, locking models featuring full locking (the Gamma model) or little locking (the Gaussian model) at the deformation front can provide the same fit to the land-based GNSS data. Here we further demonstrate this near-trench ambiguity using our viscoelastic model. The results are summarized in Figure 6. In these models, by limiting the back slip rate of the shallowest fault patches (roughly the most updip 10 km of the fault) to a value less than the subduction rate, we enforce some trench creep. Note that trench creep is allowed in all our models but is not always enforced, such as for the models shown in Figure 4.

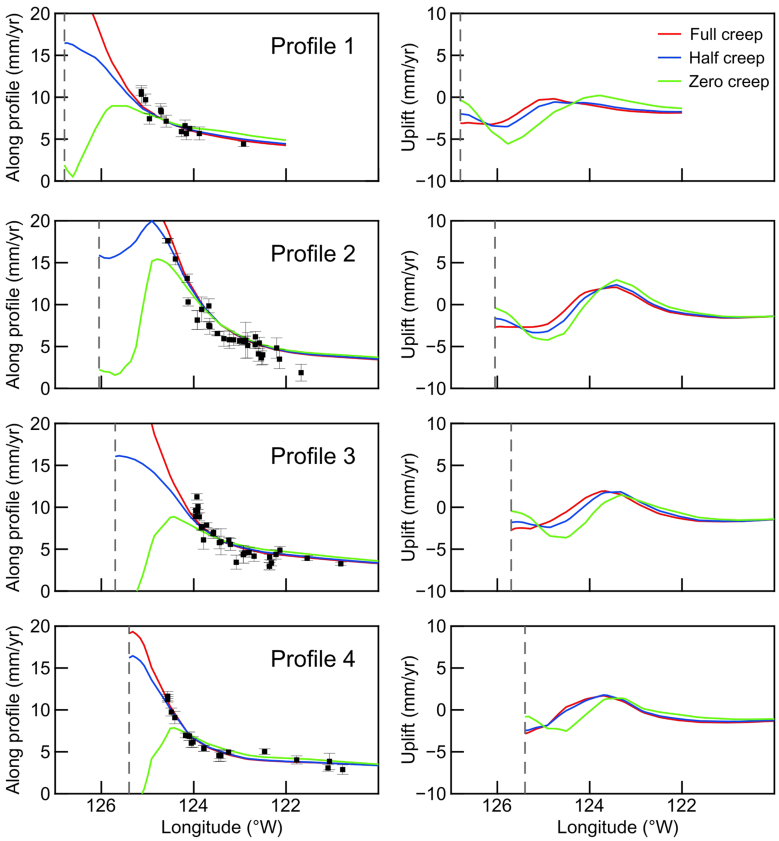

Figure 7. Surface velocities along four profiles (locations shown in Figure 6b) predicted by three viscoelastic models with different amounts of enforced trench creep and comparison with Global Navigation Satellite Systems (GNSS) data. Maximum back slip rate allowed at the deformation front is 0, 20, and 40 mm/yr for the full, half, and zero creep models, respectively. The GNSS data are from an ~30-km wide corridor along each profile. Only horizontal components of the GNSS data were used for the inversion. The error bars for the GNSS data represent one standard deviation measurement uncertainty. The dashed gray line marks the location of the deformation front.

Figures 6a and 6b show the results of a viscoelastic model in which the back slip rate at the deformation front is limited to be no greater than 20 mm/yr, representing creeping at half the subduction rate or faster. The only inversion constraint that is different from those for the models shown in Figure 4 is the limiting slip-deficit (back slip) rate allowed at the deformation front (Table 1). The model fits the GNSS data almost as well as the preferred model of Figure 4a, with RMS = 1.3 mm/yr (Figure 6a). It is important to point out, despite the near-trench ambiguity, that the viscoelastic models shown in Figures 4a and 6a are both devoid of the deep locking seen in the elastic model of Figure 4b. The main point of the paper discussed in section 4.1 is not affected by the near-trench ambiguity.

Figures 6c and 6d summarize the data misfit of the viscoelastic models with various degrees of enforced trench creep by inverting either the SMM-corrected or WWW-corrected GNSS data. Because the value of the smoothness factor also affects the misfit, we show results for a value of 400 as in the preferred model (Figure 4a) and for a value of 800 (smoother). The effect of the smoothness factor will be further discussed in section 4.3. Overall, the inversion tends to favor no or less trench creep, but the difference in data fit between having no enforced creep and having some enforced creep (such as a maximum back slip rate of 20 or 30 mm/yr) is quite small, regardless of which block-motion model is used to correct the GNSS data.

Using four trench-normal profiles with locations indicated in Figure 6b, we further illustrate how various degrees of enforced trench creep affect data fit (Figure 7). With either full, half (20 mm/yr back slip rate), or zero enforced creep, the models fit the land-based horizontal GNSS data equally well, but the results also show that the land-based GNSS observations have very limited resolving power far offshore. More

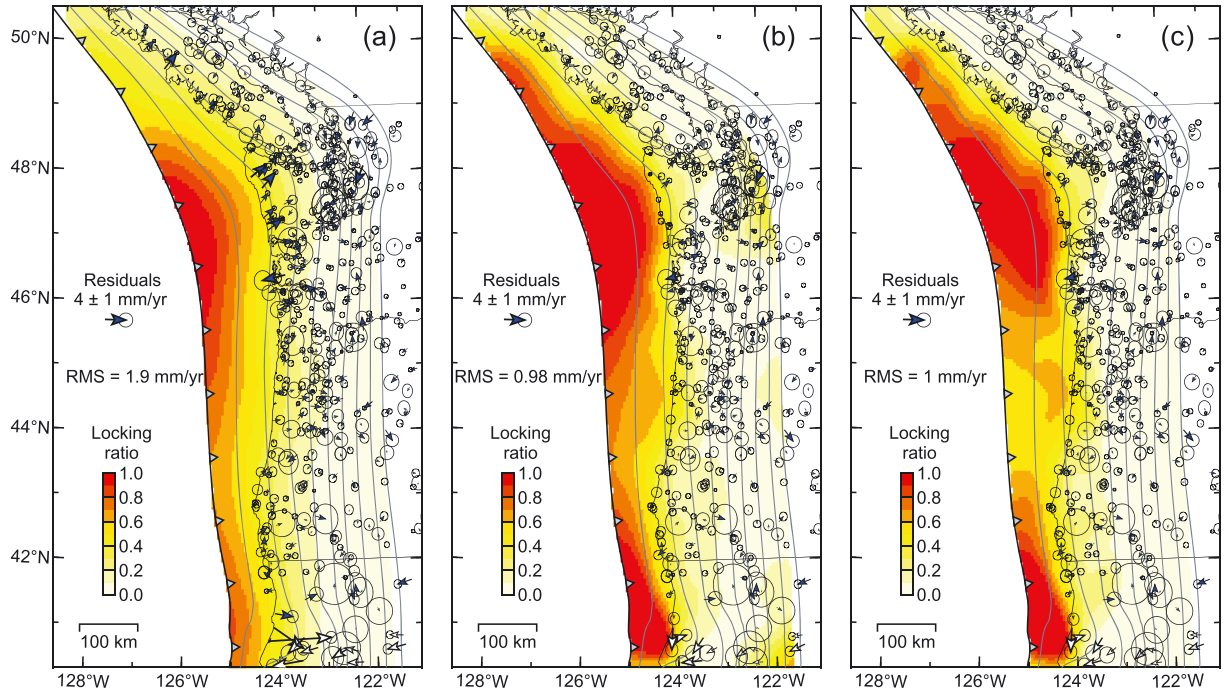

Figure 8. Examples of other viscoelastic locking models that also fit the Global Navigation Satellite Systems (GNSS) data to illustrate the effect of assumed smoothness factor β. Full locking is allowed at the trench, and the SMM model (Figure 2a) is used to correct the GNSS data (Table 1). (a) Same as the preferred model (Figure 4a) except β = 1,600. (b) Same as the preferred model (Figure 4a) except β = 100. (c) With β = 40 and limiting locking depth = 30 km, a model can be obtained to feature a creeping segment off Oregon similar to that of Schmalzle et al. (2014).

importantly, they demonstrate that even a few additional GNSS seafloor sites would dramatically improve the situation and help to identify which of these "competing" models better reflects reality. The importance of having seafloor GNSS observations in resolving megathrust locking has been demonstrated in the Nankai subduction zone with a rather uniform distribution of seafloor sites that illuminates mostly along-strike variations of interseismic seafloor velocities (Yokota et al., 2016). The results in Figure 7 as well as Figure 6 indicate that a more strategically designed site distribution that targets both along-strike and trench-normal variations will yield more diagnostic observational constraints for megathrust locking.

For both onshore and offshore, the model-predicted vertical velocity values are much smaller than the horizontal values (Figure 7). In terms of resolving near-trench locking, seafloor vertical observations may not be as diagnostic as seafloor horizontal observations. However, not reflected by the models in this work, continuous monitoring of vertical deformation and tilt offshore with seafloor and borehole pressure sensors and tilt meters is invaluable for detecting fault slip transients (e.g., Wallace et al., 2016). The slip transients or slow slip events are creep pulses and offer critically important information on the locking or creeping state of the megathrust.

4.3. Further Discussion

The present study aims to address the issue of interseismic stress relaxation by invoking more realistic Earth rheology. However, the improved Earth model by no means solves the problem of non-uniqueness of the inverse problem. In the preceding sections, we have illustrated the effects of imposing different LLD values and/or trench-creep rates on the inferred locking pattern. Here we further discuss the effects of the smoothness factor β and the type of block-motion models used for correcting the GNSS data.

The smoothness of the slip distribution is a crude description of the spatial correlation between slip vectors. The choice of the value of β thus reflects the researchers' own understanding of how sharply and smoothly the slip should vary along the fault surface. Given the ill-posedness of the inverse problem and the lack of offshore

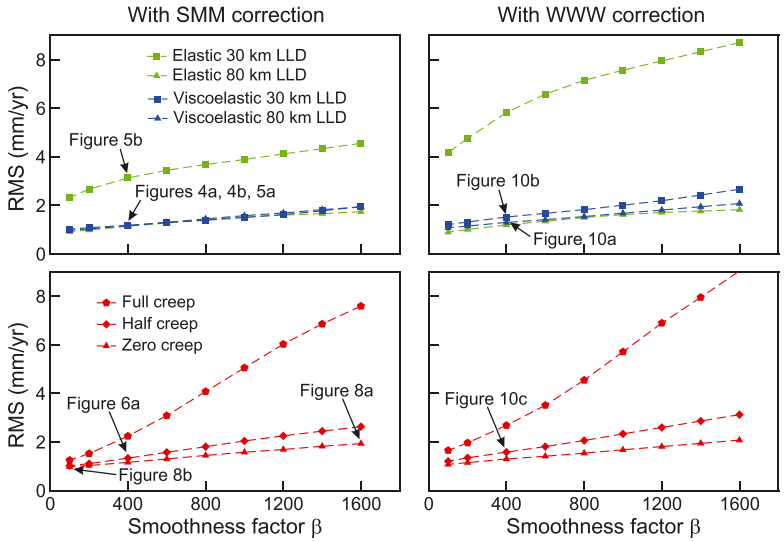

Figure 9. Effects of the smoothness factor on root-mean-square (RMS) residual of Global Navigation Satellite Systems data fit. For each block-motion model, the upper panel shows the results of elastic and viscoelastic models with either 80- or 30-km limiting locking depth (LLD), and the lower panel shows the results of viscoelastic models with 80-km LLD but different trench-creep rates. Full, half, and zero creep mean maximum back slip rates at the deformation front are limited not to exceed 0, 20, and 40 mm/yr, respectively.

constraints, it is natural that different researchers may prefer different degrees of smoothness and derive somewhat different patterns of megathrust locking from the same geodetic observations. Our preferred model uses β = 400 (Figure 4a). Figures 8a and 8b show how the locking pattern is affected if we increase or decrease the value by a factor of 4 while keeping all the other inversion parameters unchanged (Table 1). Not surprisingly, a higher β value (Figure 8a) results in a smoother locking pattern but worse data fit, and a lower value (Figure 8b) results in a more rugged locking pattern but better data fit. Because greater smoothing causes slip vectors farther apart in both the dip and strike directions to be similar, the high β value of 1,600 results in more creep at the trench (to be more similar to the deeper part of the fault; Figure 8a). Anisotropic smoothing with greater smoothing along strike but less in the dip direction (e.g., Dragert & Wang, 2011) would yield more realistic results, but it cannot be accomplished with the computer code used in this work. This is a factor contributing to our choice of using a value of 400 for β in the preferred model.

Nonetheless, the locking distributions show some robust features even with very different smoothness factors: The locking ratio decreases northward north of 49°N, is high between 46°N and 48°N, and is low in central or southern Cascadia but not in the same area as the creeping segment of Schmalzle et al. (2014). If we use β = 40 in conjunction with LLD = 30 km, we can produce a creeping segment more similar to that of Schmalzle et al. (2014; Figure 8c).

Figure 9 illustrates the effect of the smoothness factor on data fit in a fuller manner and for various LLDs, different amounts of enforced trench creep, two different Earth rheology models (elastic versus viscoelastic), and two block motion correction models (SMM versus WWW) for the GNSS data. Given Earth rheology, the level of RMS residuals is controlled more strongly by the LLD and enforced trench creep than by the smoothness factor, unless full-rate creep is imposed at the deformation front.

As discussed in section 2, there is ambiguity and uncertainty in defining long-term deformation of the upper plate. We choose to use the SMM block-motion model to correct the GNSS data for the long-term motion. To illustrate how the correction affects inversion results, we also consider the WWW block-motion model. The overall performance of the WWW correction in terms of the RMS of GNSS velocity residuals has been illustrated in Figures 5d, 6d, and 9. In Figure 10, we show the map view of three representative viscoelastic models based on the WWW correction for a more detailed comparison with those based on the SMM correction. Except for the different block-motion correction, the models in Figures 10a, 10b, and 10c are derived in

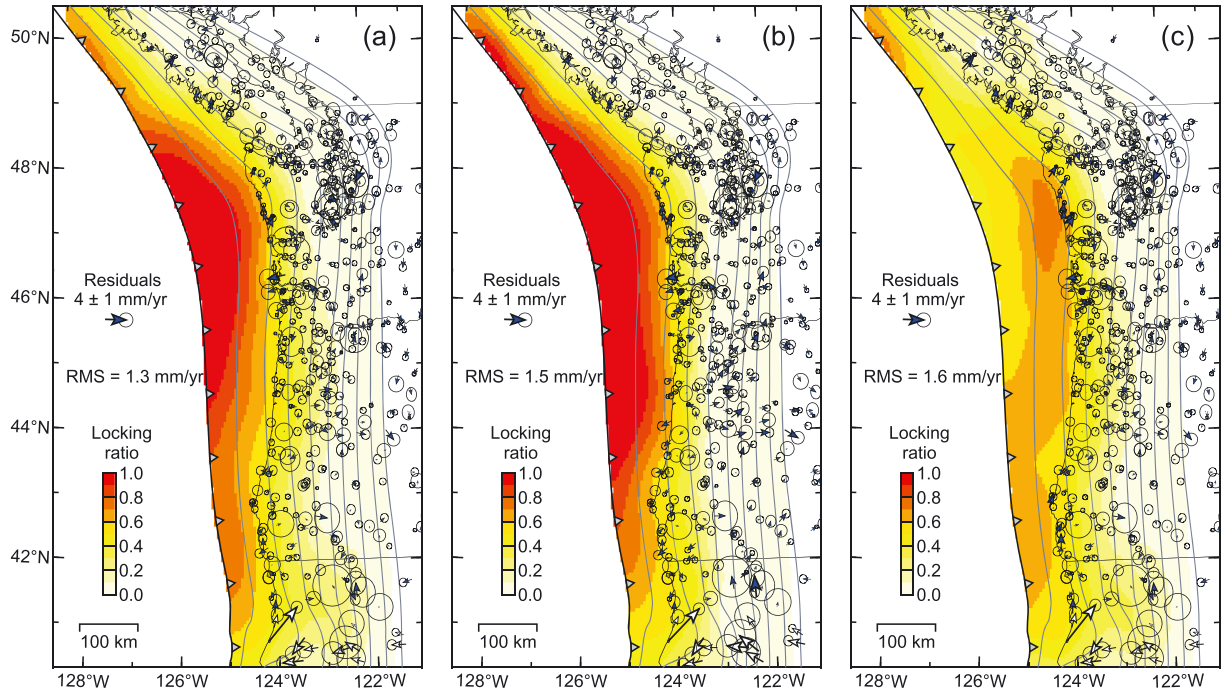

Figure 10. Examples of viscoelastic locking models by inverting Global Navigation Satellite Systems data corrected with the WWW block model (Figure 2b). (a) WWW version of the preferred model of Figure 4a. (b) WWW version of the model shown in Figure 5a (limiting locking depth = 30 km). (c) WWW version of the model shown in Figure 6a, with maximum 20-mm/yr back slip at the deformation front.

exactly the same way as the models in Figures 4a, 5a, and 6a, respectively (Table 1). Their overall locking patterns are similar to their SMM counterparts. The largest difference occurs in the southernmost part the model area, where the two types of correction show the greatest difference (Figure 2). All the discussions based on the SMM-based models regarding the roles of the LLD, enforced trench creep, smoothness factors, and, above all, the importance of interseismic viscoelastic stress relaxation apply to the WWW-based models.

The assumed viscosity values of the continental mantle (10^{19} Pa s) and oceanic mantle (10^{20} Pa s) for all the models presented in this paper are based on earlier subduction zone earthquake cycle modeling work and relevant literature (Wang, Hu, et al., 2012). To illustrate partially how uncertainties in mantle rheology may affect our results, we show in Figure S4 GNSS site velocities predicted with the continental mantle viscosity value changed by a factor of 5 or 0.5. The lower viscosity leads to almost no change to the results. For the higher viscosity, we run the model to 25 Maxwell times (1,500 years), so that the results are comparable to those of the lower viscosities. For the scenario of very shallow locking such as in the preferred model (Figure 4a), increasing the viscosity by a factor of 5 makes practically no difference (Figure S4). For deeper locking due to imposed full-rate creep of the shallow fault (Figure S4), a scenario we consider much less reasonable, the higher viscosity results in slower site motion, which means that a slightly higher locking ratio would be inferred from the same GNSS data. Of course, with such high viscosity values, the situation would be more complex because it would take much longer to relax the stress induced by the previous earthquake. Given the large ambiguity of the locking state due to the lack of seafloor constraints, we are not in a position to offer meaningful insights as to how the inversion results might be improved by including spatial and temporal viscosity variations.

A common way to illustrate "resolution" of inversion models involves the use of checkerboard tests. We have carried out checkerboard tests for our inversions. However, given the large ambiguities caused by the lack of near-field constraints as illustrated by the many examples so far discussed, we do not think the checkerboard results are very useful and hence do not display them here.

5. Conclusions

Most models of interseismic locking state of megathrust faults worldwide are derived from geodetic data using an elastic Earth model. The neglect of viscoelastic stress relaxation in these models leads to an overprediction of locking depth and/or failure to explain far-field, long-wavelength crustal deformation. The problem is particularly obvious for subduction zones that are at a late-stage of interseismic locking such as Cascadia at present (Wang & Tréhu, 2016) and the Japan Trench prior to the Tohoku-oki earthquake (Wang et al., 2018). Based on our results of inverting GNSS data to infer the locking state of the Cascadia megathrust using a finite element viscoelastic model, we draw the following conclusions:

1. Locking models based on the viscoelastic rheology are more consistent with known physical processes of subduction earthquake cycles than are elastic models. Until offshore geodetic measurements provide critically needed additional constraints, the model of high degrees of locking at shallow depths shown in Figure 4a is regarded as a preferred working model. We are mindful that the locking ratio is a kinematic description of the rate of motion; it should not be directly translated to spatial variations in frictional properties and shear stress or directly used without further analysis to predict patterns of future megathrust rupture, particularly in the dip direction.
2. For inversion models using the viscoelastic Earth rheology, the assigned LLD is unimportant. Even with an LLD of 80 km, high locking ratios tend to be confined to less than 20-km depths. Deeper locking is not needed because far-field crustal deformation is explained by interseismic stress relaxation.
3. Regardless of Earth rheology, the lack of offshore, near-field geodetic constraints leads to severe ambiguity in the locking state of the shallowest part of the megathrust. Our model results imply that even a small number of strategically located seafloor GNSS sites would revolutionize the knowledge of shallow locking or creeping at Cascadia. Seafloor measurements of vertical velocities averaged over a few years or longer will not be as diagnostic as horizontal velocities in constraining shallow locking (illustrated in Figure 7a), but continuous monitoring of vertical deformation for the purpose of detecting transient events will provide important information (not illustrated in this paper).
4. Regardless of the Earth rheology, assumed smoothness of the locking distribution affects details of the locking pattern obtained by the inversion, especially the presence and locations of creeping segments. The preferred model in Figure 4a features moderate smoothness. Only near-field, seafloor observations can constrain the actual smoothness and along-strike variations of the locking state.
5. Long-term deformation of the upper plate is and will remain to be a source of uncertainty for Cascadia megathrust locking models. For the purpose of demonstrating the importance of interseismic stress relaxation, the two tested block-motion models (Figure 2) lead to the same conclusions.

Acknowledgments

All the data used in this work have been previously published, and references are provided in the paper. Shaoyang Li was supported by a fellowship granted by the Helmholtz Graduate Research School GeoSim and conducted most of the modeling during a visit to the University of Victoria and the Pacific Geoscience Centre. We thank Dawei Gao for providing the updated fault geometry of Cascadia subduction zone. Comments from David Schmidt and an anonymous reviewer helped to improve the paper. Most of the figures in this paper are generated with the GMT software (Wessel & Smith, 1998). This is Geological Survey of Canada contribution 20180105.

References

Aagaard, B. T., Knepley, M. G., & Williams, C. A. (2013). A domain decomposition approach to implementing fault slip in finite-element models of quasi-static and dynamic crustal deformation. *Journal of Geophysical Research: Solid Earth*, *118*, 3059–3079. https://doi.org/10.1002/jgrb.50217

Atwater, B. F. (1987). Evidence for great Holocene earthquakes along the outer coast of Washington State. *Science*, *236*(4804), 942–944. https://doi.org/10.1126/science.236.4804.942

Atwater, B. F., & Hemphill-Haley, E. (1997). Recurrence intervals for great earthquakes of the past 3,500 years at northeastern Willapa Bay, Washington (no. 1576). USGPO; information services (distributor).

Bott, M. H. P., & Dean, D. S. (1973). Stress diffusion from plate boundaries. *Nature*, *243*(5406), 339–341. https://doi.org/10.1038/243339a0

Cohen, S. C. (1984). Postseismic deformation due to subcrustal viscoelastic relaxation following dip-slip earthquakes. *Journal of Geophysical Research*, *89*, 4538–4544. https://doi.org/10.1029/JB089iB06p04538

Coleman, T. F., & Li, Y. (1996). A reflective Newton method for minimizing a quadratic function subject to bounds on some of the variables. *SIAM Journal on Optimization*, *6*(4), 1040–1058. https://doi.org/10.1137/S1052623494240456

DeMets, C., Gordon, R. G., & Argus, D. F. (2010). Geologically current plate motions. *Geophysical Journal International*, *181*(1), 1–80. https://doi.org/10.1111/j.1365-246X.2009.04491.x

van Dinther, Y., Gerya, T. V., Dalguer, L. A., Mai, P. M., Morra, G., & Giardini, D. (2013). The seismic cycle at subduction thrusts: Insights from seismo-thermo-mechanical models. *Journal of Geophysical Research: Solid Earth*, *118*, 6183–6202. https://doi.org/10.1002/2013JB010380

Dragert, H., & Wang, K. (2011). Temporal evolution of an episodic tremor and slip event along the northern Cascadia margin. *Journal of Geophysical Research*, *116*, B12406. https://doi.org/10.1029/2011JB008609

Dragert, H., Wang, K., & James, T. S. (2001). A silent slip event on the deeper Cascadia subduction interface. *Science*, *292*(5521), 1525–1528. https://doi.org/10.1126/science.1060152

Elsasser, W. M. (1969). Dynamic processes in upper earth mantle, discussing thermal convection currents and stress propagation. In S. K. Runcorn (Ed.), *The application of modern physics to the Earth and planetary interiors* (pp. 223–246). New York: John Wiley.

Gao, D. (2016). *Defining megathrust tsunami sources at northernmost Cascadia using thermal and structural information* (Master's thesis, University of Victoria, Victoria, Canada). Retrieved from http://hdl.handle.net/1828/7435

Gao, D., Wang, K., Davis, E. E., Jiang, Y., Insua, T. L., & He, J. (2017). Thermal state of the Explorer segment of the Cascadia subduction zone: Implications for seismic and tsunami hazards. *Geochemistry, Geophysics, Geosystems*, *18*, 1569–1579. https://doi.org/10.1002/2017GC006838

Gao, X., & Wang, K. (2017). Rheological separation of the megathrust seismogenic zone and episodic tremor and slip. *Nature*, *543*(7645), 416–419. https://doi.org/10.1038/nature21389

Goldfinger, C., Galer, S., Beeson, J., Hamilton, T., Black, B., Romsos, C., et al. (2017). The importance of site selection, sediment supply, and hydrodynamics: A case study of submarine paleoseismology on the northern Cascadia margin, Washington USA. *Marine Geology*, *384*, 4–46. https://doi.org/10.1016/j.margeo.2016.06.008

Henton, J. A. (2000). *GPS studies of crustal deformation in the northern Cascadia subduction zone* (PhD thesis, University of Victoria, B. C., Canada.

Hyndman, R. D., & Wang, K. (1993). Thermal constraints on the zone of major thrust earthquake failure: The Cascadia subduction zone. *Journal of Geophysical Research*, *98*, 2039–2060. https://doi.org/10.1029/92JB02279

Khazaradze, G., Qamar, A., & Dragert, H. (1999). Tectonic deformation in western Washington from continuous GPS measurements. *Geophysical Research Letters*, *26*, 3153–3156. https://doi.org/10.1029/1999GL010458

Leonard, L. J., Currie, C. A., Mazzotti, S., & Hyndman, R. D. (2010). Rupture area and displacement of past Cascadia great earthquakes from coastal coseismic subsidence. *GSA Bulletin*, *122*(11–12), 2079–2096. https://doi.org/10.1130/B30108.1

Li, S., Moreno, M., Bedford, J., Rosenau, M., & Oncken, O. (2015). Revisiting viscoelastic effects on interseismic deformation and locking degree: A case study of the Peru-North Chile subduction zone. *Journal of Geophysical Research: Solid Earth*, *120*, 4522–4538. https://doi.org/10.1002/2015JB011903

Matsu'ura, M., & Sato, T. (1989). A dislocation model for the earthquake cycle at convergent plate boundaries. *Geophyscal Journal International*, *96*(1), 23–32. https://doi.org/10.1111/j.1365-246X.1989.tb05247.x

Mazzotti, S., Dragert, H., Henton, J., Schmidt, M., Hyndman, R. D., James, T., et al. (2003). Current tectonics of northern Cascadia from a decade of GPS measurements. *Journal of Geophysical Research*, *108*(B12), 2554. https://doi.org/10.1029/2003JB002653

McCaffrey, R., King, R. W., Payne, S. J., & Lancaster, M. (2013). Active tectonics of northwestern U.S. inferred from GPS-derived surface velocities. *Journal of Geophysical Research: Solid Earth*, *118*, 709–723. https://doi.org/10.1029/2012JB009473

McCaffrey, R., Qamar, A. I., King, R. W., Wells, R., Khazaradze, G., Williams, C. A., et al. (2007). Fault locking, block rotation and crustal deformation in the Pacific Northwest. *Geophysical Journal International*, *169*(3), 1315–1340. https://doi.org/10.1111/j.1365-246X.2007.03371.x

McCrory, P. A., Blair, J. L., Oppenheimer, D. H., & Walter, S. R. (2004). Depth to the Juan de Fuca slab beneath the Cascadia subduction margin: A 3-D model for sorting earthquakes. U.S. Department of the Interior, U.S. Geological Survey.

McCrory, P. A., Blair, J. L., Waldhauser, F., & Oppenheimer, D. H. (2012). Juan de Fuca slab geometry and its relation to Wadati-Benioff zone seismicity. *Journal of Geophysical Research*, *117*, B09306. https://doi.org/10.1029/2012JB009407

Miller, M. M., Johnson, D. J., Rubin, C. M., Dragert, H., Wang, K., Qamar, A., & Goldfinger, C. (2001). GPS-determination of along-strike variation in Cascadia margin kinematics: Implications for relative plate motion, subduction zone coupling, and permanent deformation. *Tectonics*, *20*, 161–176. https://doi.org/10.1029/2000TC001224

Miyashita, K. (1987). A model of plate convergence in southwest Japan, inferred from levelling data associated with the 1946 Nankaido earthquake. *Journal of Physics of the Earth*, *35*(6), 449–467. https://doi.org/10.4294/jpe1952.35.449

Okada, Y. (1992). Internal deformation due to shear and tensile faults in a half-space. *Bulletin of the Seismological Society of America*, *82*(2), 1018–1040.

Pollitz, F. F. (2003). Transient rheology of the uppermost mantle beneath the Mojave Desert, California. *Earth and Planetary Science Letters*, *215*(1–2), 89–104. https://doi.org/10.1016/S0012-821X(03)00432-1

Pollitz, F. F., & Evans, E. L. (2017). Implications of the earthquake cycle for inferring fault locking on the Cascadia megathrust. *Geophysical Journal International*, *209*(1), 167–185. https://doi.org/10.1093/gji/ggx009

Rogers, G., & Dragert, H. (2003). Episodic tremor and slip on the Cascadia subduction zone: The chatter of silent slip. *Science*, *300*(5627), 1942–1943. https://doi.org/10.1126/science.1084783

Royer, A. A., & Bostock, M. G. (2014). A comparative study of low frequency earthquake templates in northern Cascadia. *Earth and Planetary Science Letters*, *402*, 247–256. https://doi.org/10.1016/j.epsl.2013.08.040

Satake, K., Wang, K., & Atwater, B. F. (2003). Fault slip and seismic moment of the 1700 Cascadia earthquake inferred from Japanese tsunami descriptions. *Journal of Geophysical Research: Solid Earth*, *108*(B11), 2535. https://doi.org/10.1029/2003JB002521

Savage, J. C. (1983). A dislocation model of strain accumulation and release at a subduction zone. *Journal of Geophysical Research*, *88*, 4984–4996. https://doi.org/10.1029/JB088iB06p04984

Savage, J. C., Lisowski, M. M., & Prescott, W. H. (1991). Strain accumulation in western Washington. *Journal of Geophysical Research*, *96*, 14,493–14,507. https://doi.org/10.1029/91JB01274

Schmalzle, G. M., McCaffrey, R., & Creager, K. C. (2014). Central Cascadia subduction zone creep. *Geochemistry, Geophysics, Geosystems*, *15*, 1515–1532. https://doi.org/10.1002/2013GC005172

Sobolev, S. V., & Muldashev, I. A. (2017). Modeling seismic cycles of great megathrust earthquakes across the scales with focus at postseismic phase. *Geochemistry, Geophysics, Geosystems*, *18*, 4387–4408. https://doi.org/10.1002/2017GC007230

Thatcher, W., & Rundle, J. B. (1984). A viscoelastic coupling model for the cyclic deformation due to periodically repeated earthquakes at subduction zones. *Journal of Geophysical Research*, *89*, 7631–7640. https://doi.org/10.1029/JB089iB09p07631

Wald, D. J., & Heaton, T. H. (1994). Spatial and temporal distribution of slip for the 1992 Landers, California, earthquake. *Bulletin of the Seismological Society of America*, *84*(3), 668–691.

Wallace, L. M., Webb, S. C., Ito, Y., Mochizuki, K., Hino, R., Henrys, S., et al. (2016). Slow slip near the trench at the Hikurangi subduction zone, New Zealand. *Science*, *352*(6286), 701–704. https://doi.org/10.1126/science.aaf2349

Wang, K. (1995). Coupling of tectonic loading and earthquake fault slips at subduction zones. *Pure and Applied Geophysics*, *145*(3-4), 537–559. https://doi.org/10.1007/BF00879588

Wang, K., Dragert, H., & Melosh, H. J. (1994). Finite element study of uplift and strain across Vancouver Island. *Canadian Journal of Earth Sciences*, *31*(10), 1510–1522. https://doi.org/10.1139/e94-134

Wang, K., He, J., Dragert, H., & James, T. (2001). Three-dimensional viscoelastic interseismic deformation model for the Cascadia subduction zone. *Earth, Planets and Space*, *53*(4), 295–306. https://doi.org/10.1186/BF03352386

Wang, K., Hu, Y., & He, J. (2012). Deformation cycles of subduction earthquakes in a viscoelastic Earth. *Nature*, *484*(7394), 327–332. https://doi.org/10.1038/nature11032

Wang, K., Sun, T., Brown, L., Hino, R., Tomita, F., Kido, M., et al. (2018). Learning from crustal deformation associated with the M=9 2011 Tohoku-oki earthquake. *Geosphere*, *14*(2), 552–571. https://doi.org/10.1130/GES01531.1

Wang, K., & Tréhu, A. M. (2016). Invited review paper: Some outstanding issues in the study of great megathrust earthquakes—The Cascadia example. *Journal of Geodynamics*, *98*, 1–18. https://doi.org/10.1016/j.jog.2016.03.010

Wang, K., Wells, R., Mazzotti, S., Hyndman, R. D., & Sagiya, T. (2003). A revised dislocation model of interseismic deformation of the Cascadia subduction zone. *Journal of Geophysical Research*, *108*(B1), 2026. https://doi.org/10.1029/2001JB001227

Wang, P.-L., Engelhart, S. E., Wang, K., Hawkes, A. D., Horton, B. P., Nelson, A. R., & Witter, R. C. (2013). Heterogeneous rupture in the great Cascadia earthquake of 1700 inferred from coastal subsidence estimates. *Journal of Geophysical Research: Solid Earth*, *118*, 2460–2473. https://doi.org/10.1002/jgrb.50101

Wang, Y., Wang, K., & He, J. (2012). On the possibility of interseismic creep of the Cascadia megathrust. Abstract T23E-2717, 2012 fall meeting, AGU, San Francisco, CA, 10–14 Dec.

Wells, R. E., Blakely, R. J., Wech, A. G., McCrory, P. A., & Michael, A. (2017). Cascadia subduction tremor muted by crustal faults. *Geology*, *45*(6), 515–518. https://doi.org/10.1130/G38835.1

Wells, R. E., & Simpson, R. W. (2001). Northward migration of the Cascadia forearc in the northwestern U.S. and implications for subduction deformation. *Earth, Planets and Space*, *53*(4), 275–283. https://doi.org/10.1186/BF03352384

Wells, R. E., Weaver, C. S., & Blakely, R. J. (1998). Fore-arc migration in Cascadia and its neotectonic significance. *Geology*, *26*(8), 759–762. https://doi.org/10.1130/0091-7613(1998)026<0759:FAMICA>2.3.CO;2

Wessel, P., & Smith, W. H. (1998). New, improved version of Generic Mapping Tools released. *Eos, Transactions American Geophysical Union*, *79*(47), 579–579. https://doi.org/10.1029/98EO00426

Yokota, Y., Ishikawa, T., Watanabe, S. I., Tashiro, T., & Asada, A. (2016). Seafloor geodetic constraints on interplate coupling of the Nankai trough megathrust zone. *Nature*, *534*(7607), 374–377. https://doi.org/10.1038/nature17632